

# Analysis of Tapered Nanopillars for Reflective Metalens: The Role of Higher-Order Modes

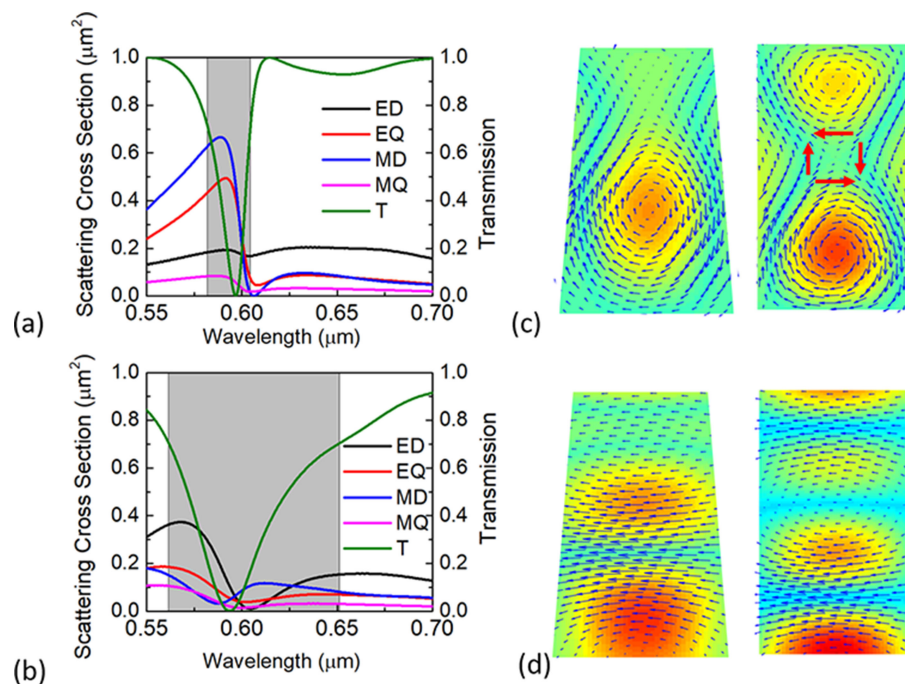
Volume 12, Number 4, August 2020

Ronghui Lin, *Member, IEEE*

Zahrah Alnakhli

Feras AlQatari

Xiaohang Li, *Member, IEEE*



DOI: 10.1109/JPHOT.2020.3007489

# Analysis of Tapered Nanopillars for Reflective Metalens: The Role of Higher-Order Modes

Ronghui Lin , Member, IEEE, Zahrah Alnakhli, Feras AlQatari, and Xiaohang Li , Member, IEEE

Advanced Semiconductor Laboratory, King Abdullah University of Science and Technology (KAUST), Thuwal 23955-6900, Saudi Arabia

DOI:10.1109/JPHOT.2020.3007489

This work is licensed under a Creative Commons Attribution 4.0 License. For more information, see <https://creativecommons.org/licenses/by/4.0/>

Manuscript received June 8, 2020; revised June 27, 2020; accepted July 2, 2020. Date of publication July 7, 2020; date of current version July 20, 2020. This work was supported by KAUST Baseline Fund BAS/1/1664-01-01, and Competitive Research Grants URF/1/3437-01-01 and URF/1/3771-01-01. Corresponding author: Xiaohang Li (e-mail: xiaohang.li@kaust.edu.sa).

**Abstract:** Despite the widespread interest in the metalens technology, few works show the errors during fabrication and analyze how they influence the focusing performance. In this work, we proposed a reflective metalens design and carry out a fundamental study on how a mild tapering angle ( $<6^\circ$ ) of the nanopillars would influence the performance of a reflective metalens. By analyzing the interaction of Mie resonance in the lateral direction and Fabry-Pérot resonance in the longitudinal direction using numerical simulations, we reveal the detrimental role the tapering angle plays due to the low transmission near the resonance. We observe the weakening of the electric quadrupole and magnetic dipole response, and the increase of the electric dipole response for tapered nanopillars. Moreover, the Fabry-Pérot resonance is disturbed due to the broken symmetry. These factors contribute to lower Q factor resonance and hence the low transmission. The results presented in this work can guide the analysis of fabrication errors and provide insights on how to compensate them.

**Index Terms:** Metalens, mie resonance, fabry-pérot resonance.

## 1. Introduction

The metalens allows for the subdiffraction limit manipulation of light with nanoantennas [1]. They could be fabricated using CMOS-compatible techniques facilitating the integration with other miniaturized optical and electronic devices. Integration with light source [2], multilayer metalens stackings [3], [4], and MEMS actuators [5] and various other components have been demonstrated. These integrations expand the functionality of the metalens and bring it one step closer to large scale commercialization and application. The reflective metalenses is an important part of the metasurface technology and play critical roles in applications such as imaging and metaholograms [6], [7]. However, Previous reports of the reflective metalens have mainly used metallic layers as the mirror [8]–[12], which could cause issues such as low reflectivity, high loss due to plasmonics coupling, and difficulty in fabrication.

In this work, we design a reflective metalens based on an all-dielectric distributed Bragg reflector (DBR) structure which would address the issues above. Dielectric metalenses have been shown to facilitate sub-diffraction limit light manipulation with low losses. The fundamental Mie type magnetic dipole and electric dipole resonance are widely studied in the context of metasurface and have

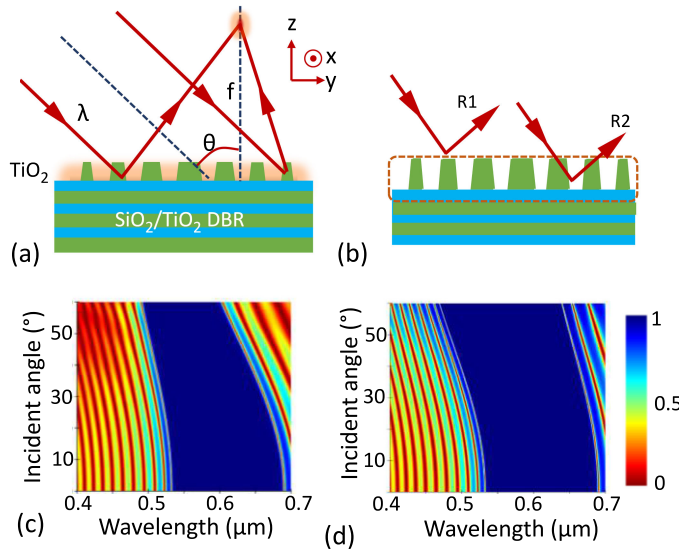


Fig. 1. (a) The proposed reflective metalens design. (b) The reflections  $R_1$  and  $R_2$  at two interfaces. (c-d) The simulated reflection spectrum for (c) TE and (d) TM incidence of light.

shown to bring rich optical phenomena [13]. However, the interaction of the higher-order modes is more complicated and less studied.

It has been shown that the interaction of the high order multipole components leads to meta devices with interesting properties such as broadband operation [14], high transmission [15], and scattering direction control [16]. The constituent elements of a dielectric metasurface are nanostructures with a high aspect ratio where the height is comparable to the design wavelength to ensure a  $2\pi$  phase coverage [1]; and the lateral dimensions are much smaller than the wavelength to ensure a smooth phase profile [17]. Such a particular size combination leads to the interaction of the Mie type resonance in the lateral direction and higher-order Fabry-Pérot type resonance in the height dimension [18].

One question arises from such a scenario: What is the implication of a tapering angle? Does it play a role in the performance of the device? Despite the widespread interest in the metasurface, these questions have not been addressed, especially in a theoretical framework that reveals the physical insights. Moreover, it is inevitable during the fabrication process to have a mild tapering angle because of the high aspect ratio and the need for faster and cheaper fabrication methods for large scale production, as is evident in previous publications [19]–[21]. Such a tapering angle is often hard to be controlled by fabrication so the numerical simulation is a powerful tool to understand the nuance these tapering angles might bring. By numerical simulation, we show in this study that even a moderate tapering angle of ( $<6^\circ$ ) degrees would deteriorate the metasurface performance. The mechanism of deterioration can be understood from the low transmission near the resonance. By adopting the multipole expansion method, we reveal the unique optical properties as a consequence of the interaction of Mie type and Fabry-Pérot type resonances and the detrimental role the tapered nanopillars play in the metasurface.

## 2. Simulation Details and Results

Fig. 1 shows the schematic of the proposed dielectric reflective metasurface. An array of nanopillars ( $\text{TiO}_2$ ) serving as phase-shifting nanoantennas are located on top of  $\text{SiO}_2/\text{TiO}_2$  DBR layers. The DBR consists of alternating layers of  $\text{TiO}_2$  and  $\text{SiO}_2$ , each with a thickness equaling to the quarter wavelength ( $\lambda/4n$ ). The refractive indices of  $\text{TiO}_2$  and  $\text{SiO}_2$  are taken from references [22], [23]. Fig. 1(c–d) shows the reflection spectrum of the designed 20-pair DBR for both transverse electric

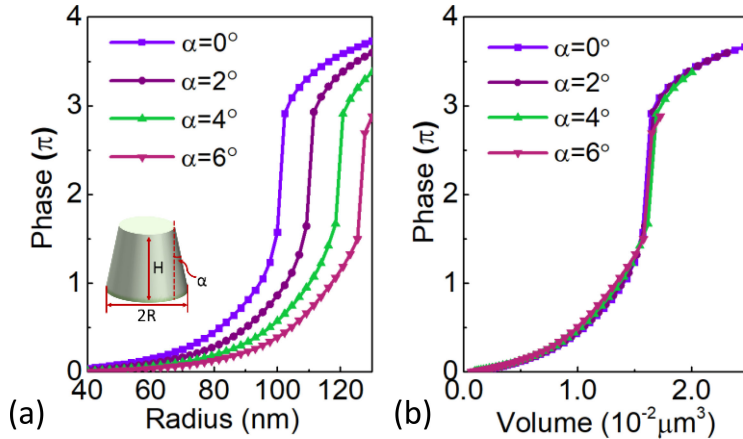


Fig. 2. The phase delay of nanopillars with different tapering angles  $\alpha$  plotted against (a) the bottom radius and (b) the volume. The inset shows the geometrical parameters of a nanopillar.

(TE) and transverse magnetic (TM) incidence. The designed wavelength is 600 nm, which is located at the center of the DBR reflection spectrum. A reflection band of 100 nm for the incident angle from  $0^\circ$  to  $60^\circ$  with reflectivity  $> 99.9\%$  is observed. This ensures a much higher reflectivity than typical metal mirrors [24]. The reflection of the proposed metalens can be broken down as Fig. 1(b) where the reflections at two interfaces are denoted as R1 and R2. Light reflection from R1 is undesirable because it does not go through phase delay, i.e. stray light. On the contrary, higher R2, which is ensured by the DBR, is desirable because this portion of the light undergoes a phase change and therefore can be focused. Intuitively, introducing a tapering angle would reduce R1 since it introduces a gradual transition of the refractive index. From this point of view, a tapering angle should be beneficial. However, our results show the opposite, which is explained in the following text.

The phase delay of a single nanopillar is determined by finite-difference time-domain (FDTD) simulation (FDTD solutions, Lumerical Inc.) using the standard setup [25]. A broadband plane wave incident on the structure and the corresponding transmission and phase delay are recorded. The phase delay is multiplied by two for the lens design because in a reflective scheme the light passes through the structure twice. The perfectly matched layer (PML) boundary condition is used in the longitudinal direction and the periodic boundary condition is employed in the transverse direction. The unit cell size  $P$  is assumed to be 400 nm to satisfy the Nyquist sampling criterion ( $P < \lambda/2NA$ ) and the nanopillar height  $H$  is set to be 500 nm. Fig. 2(a) shows the phase delay of nanopillars with different tapering angles as a function of the bottom radius. All the curves follow a similar trend: the phase increases with the radius and a jump occurs at the resonance. As the tapering angle increases, the curves shift toward a higher radius. This indicates an unwanted tapering angle during fabrication would influence the performance because the phase delay is no longer the intended value. When the phase delay is plotted against the volume, all the curves become the same, which indicates the volume is the determining factor of the phase change. This principle can be used to compensate for the error of the tapering angle during the design and fabrication of the metalens.

The reflective metalenses with the same focal length but different nanopillar tapering angles  $\alpha$  are designed based on the simulated phase delay. The size of the nanopillars are assigned based on the following phase condition:

$$\varphi_f(x, y) = \frac{2\pi}{\lambda} \left( f - \sqrt{x^2 + y^2 + f^2} \right) \quad (1)$$

where  $\lambda$  is the design wavelength,  $f$  is the focal length, and  $x, y$  are the position of the nanopillars. The phase profile is shown in Fig. 3(a), and Fig. 3(b) shows the corresponding bottom radius for the nanopillars with  $\alpha = 6^\circ$ . We simulate metalenses with an aperture size of 15  $\mu\text{m}$  and a focal

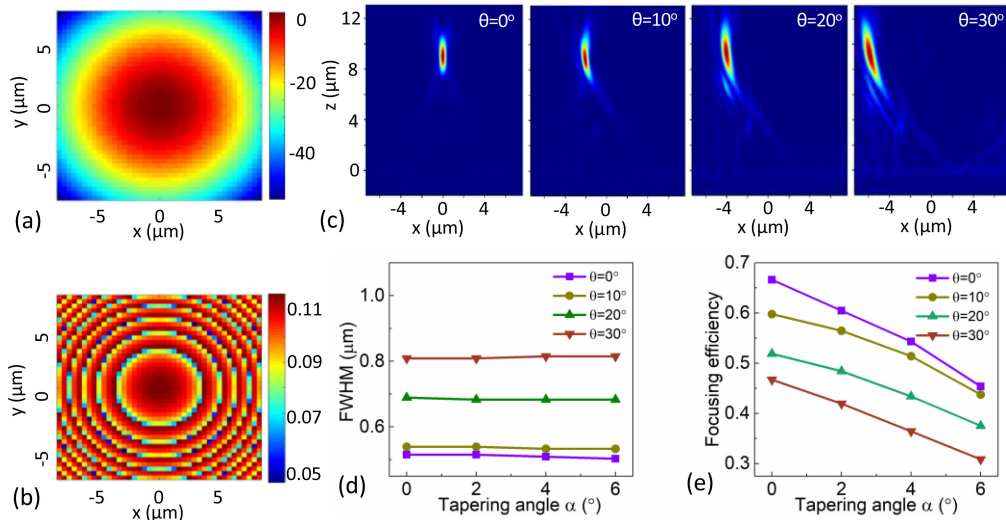


Fig. 3. (a) Phase profile for focusing metolens, the unit of the colorbar is rad. (b) The bottom radius of nanopillars with  $\alpha = 6^\circ$  for metolens design, the unit of the colorbar is  $\mu\text{m}$ . (c) Electric field intensity profiles for incident angles of  $0^\circ$ ,  $10^\circ$ ,  $20^\circ$ , and  $30^\circ$ , respectively. (d) FWHM of the focal spot for different nanopillars at different incident angles. (e) Focusing efficiency for metolenses consisting of nanopillars at different incident angles.

length of  $10 \mu\text{m}$ . The numerical apertures (NAs) are calculated to be 0.6. The FWHM of the focal points and the focusing efficiency are compared for the tapered and untapered nanopillars. The focusing efficiency is defined as the ratio of the power within a radius of  $3 \times \text{FWHM}$  area to the total incident power [8].

Fig. 3(c) manifests the electric field intensity distribution for different incident angles. The focal point shifts in the transverse direction as the incident angle changes from  $0^\circ$ ,  $10^\circ$ ,  $20^\circ$ , to  $30^\circ$ . The shifting distance follows the equation  $\Delta x = f \tan\theta$ , where  $\Delta x$  is the shift,  $f$  is the focal length, and  $\theta$  is the oblique incidence angle. At the same time, we observe an increase of the full width half maximum (FWHM) and a drop of the focusing efficiency as the incident angle is increased shown in Fig. 3(d–e). This deterioration of performance is due to the increased lateral propagation at the interface as the incident angle increases. Apart from the incident angle, the tapering angles of the nanopillars are also considered.

As shown in Fig. 3(d), the FWHM for the untapered nanopillars at normal incidence is 515 nm which is close to the diffraction limit ( $\lambda/2NA$ ) and it remains unaffected by the tapering angle. This is because the tapered pillars are designed based on the corrected phase delay exhibited in Fig. 2(b). The efficiency is greatly affected by the tapering angle shown in Fig. 3(e). At normal incidence ( $\theta = 0^\circ$ ), the focusing efficiency is 66%, which drops dramatically to 46% as the tapering angle increases to  $6^\circ$ . The same trend is observed for other incident angles from  $10^\circ$  to  $30^\circ$ .

The monotonic drop of the focusing efficiency with the increase of the tapering angle can be explained by the transmission curve in Fig. 4(a). With a small bottom radius ( $< 95 \text{ nm}$ ), the transmission is almost 1. But it drops to almost 0 at the resonant wavelength. The contrast of transmission between different tapering angles is clear when it is plotted against the volume in Fig. 4(b). The FWHM of the transmission curve increases as a result of the tapering angle. The transmission is much lower at the same volume for the tapered structures due to the low Q factor of the resonance. Therefore, the tapered structure increases R1 shown in Fig. 1(b), which results in compromised focusing efficiency.

To shed more light on the mechanism of the low Q factor for the tapered structures, we perform a multipole expansion analysis on the scattered field [26]. The contributions of the magnetic dipole (MD), electric dipole (ED), electric quadrupole (EQ), and magnetic quadrupole (MQ) are considered. Fig. 5(a–b) shows the comparison of multipole contributions of nanopillars with  $0^\circ$  and

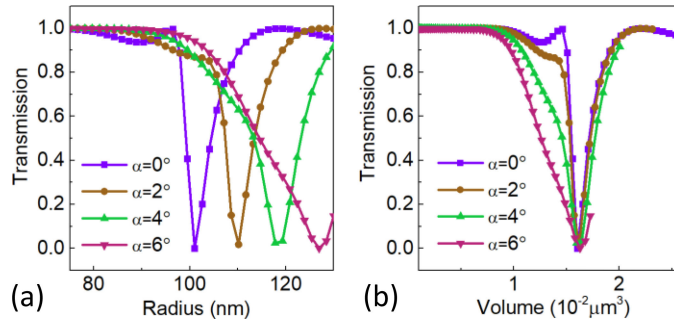


Fig. 4. Transmission of nanopillars with different tapering angles plotted against (a) the bottom radius and (b) the volume.

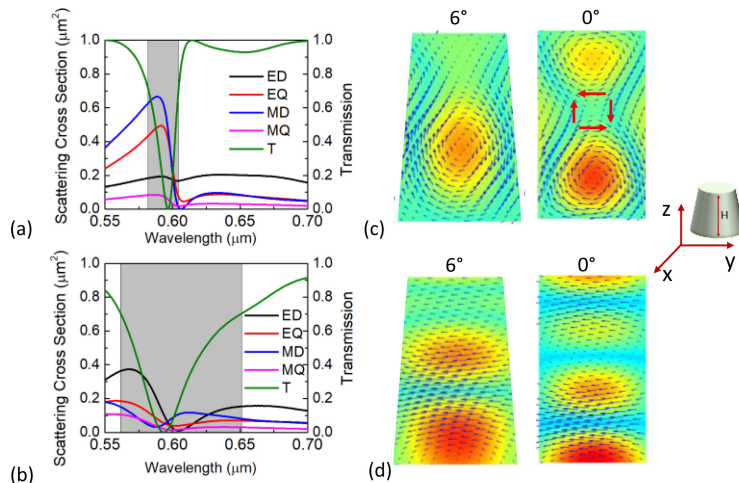


Fig. 5. (a-b) Multipole scattering contribution of (a) untapered nanopillars, (b) nanopillars with a  $6^\circ$  tapering angle. (c) Electric field vector and magnetic field magnitude contour in the XZ plane for nanopillars with a  $6^\circ$  tapering angle and untapered nanopillars. (d) Magnetic field vector and electric field magnitude contour in the YZ plane for nanopillars with a  $6^\circ$  tapering angle and untapered nanopillars.

$6^\circ$  tapering angles but a similar volume ( $1.6 \times 10^{-2} \mu\text{m}^3$ ). The shaded areas indicate the areas with a transmission of less than 70%. It is much broad for nanopillars with a  $6^\circ$  tapering angle due to the low Q factor. Within this area, the untapered nanopillars have a dominant MD and EQ response with narrower FWHMs [27]. The transmission reaches a minimum value at the resonant wavelength [28]. This arises from the satisfaction of generalized Kerker condition [29]–[31], which cancels out the forward scattering. Off resonance, the phase of these resonances quickly flips by  $\pi$ ; and the high Q modes of EQ and MD switch the direction quickly that results in high transmission. But the low Q modes of ED cannot switch direction so fast. Thus the overall transmission spectrum has a much larger FWHM for the tapered structure.

Fig. 5(c) shows the electric field vector and magnetic field intensity at the XZ cross-sections. The field distributions for untapered nanopillars are more symmetrical about the XY plane. Fig. 5(c) exhibits that the untapered nanopillar contains two loops of circulating electric field rotating in the same direction, which gives rise to a strong MD response. In between these two sets of loops, the electric current forms an MQ configuration as indicated by the red arrows. Due to this arrangement, the MD and EQ always coexist with similar peak positions as can be seen from Fig. 5(a), this overlapping of MD and EQ is an important contributor to meet Kerker condition as mentioned earlier. For the tapered nanopillar, the field distribution is different: only one loop of electric current exists and the EQ configuration is pushed toward the top of the structure with

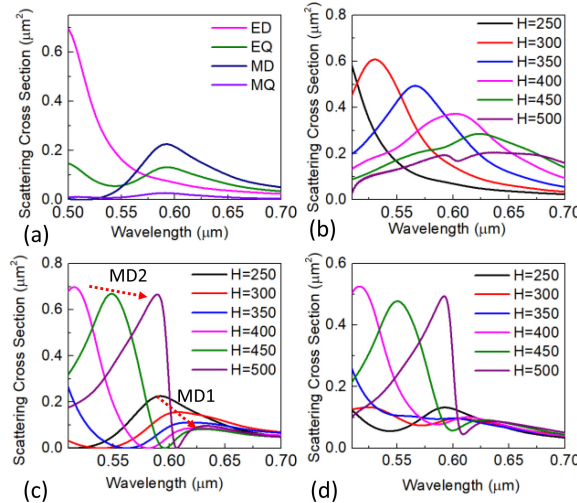


Fig. 6. (a) Multipole scattering contributions for the untapered nanopillar with height  $H = 250$  nm. (b) ED. (c) MD. (d) EQ contributions for the untapered nanopillars with increasing height  $H$  (nm).

much weaker intensity, which is a result of the broken symmetry about the XY plane. Fig. 5(d) shows the magnetic field vector and electric field intensity at the YZ cross-sections, it is clear that the Fabry-Pérot type resonance is stronger for the untapered nanopillars with evenly spaced electric field nodes. From the above discussion, we can conclude that the untampered nanopillars promote the co-existence of the MD and EQ modes which contributes to the Kerker condition, and meanwhile, it enhances vertical Fabry-Pérot type resonance. These factors contribute to a narrower FWHM in the transmission spectrum.

Here we observe enhanced MD and EQ contribution and weakened ED contribution. To show how these modes evolve, we plot the multipole contribution for the untapered nanopillars with different heights in Fig. 6. Fig. 6(a) is the multipole scattering of a cylinder with  $R = 100$  nm,  $H = 250$  nm. Due to the low aspect ratio, the major response is MD at  $\sim 600$  nm and ED at a shorter wavelength, which is similar to previous reports [32]. Fig. 6(b-d) shows how the ED, EQ, and MD evolves as the height is gradually increased. We can see a redshift of the ED with progressively lower Q factor as the height increases. Meanwhile, the EQ and MD are redshifted with progressively higher Q factor. The trend of MD and EQ is very similar due to their coexistence relationship as explained in the previous text. These plots show that the enhancement of the MD and ED is a direct consequence of the increased nanopillar aspect ratio during metolens design. Another phenomenon we observe is the existence of two magnetic modes MD1 and MD2. MD1 is the magnetic dipole with one node and MD2 is the magnetic dipole with two nodes. The distinction can be shown in Fig. 5(c). At low aspect ratios, only MD1 is shown because the height of the nanopillar cannot support two nodes. As the height increases, the intensity of MD1 becomes weaker while that of MD2 grows, with higher fineness. The appearance of MD2 can be understood easily as the increased height being able to accommodate more oscillation nodes in the vertical direction.

### 3. Conclusions

In conclusion, We propose a reflective metolens based on DBR structures with high reflectivity. By rigorous numerical simulation, we reveal the detrimental role of a small tapering angle of the nanopillars played in reflective metolens, which results from the weakening of the multipole contribution of MD and EQ and the Fabry-Pérot resonance due to the symmetry breaking. We also show the increase of ED and MD contribution is a natural consequence of the increased aspect ratio for the metolens design. The results presented in this paper can guide the analysis of fabrication errors and provide insights on how to compensate them.

## References

- [1] M. Khorasaninejad and F. Capasso, "Metalenses: Versatile multifunctional photonic components," *Science*, vol. 358, no. 6367, 2017, Art. no. eaam8100.
- [2] Y. Y. Xie *et al.*, "Metasurface-integrated vertical cavity surface-emitting lasers for programmable directional lasing emissions," *Nature Nanotechnol.*, vol. 15, no. 2, pp. 125–130, 2020.
- [3] R.H. Lin and X.H. Li, "Multifocal metalens based on multilayer Pancharatnam-Berry phase elements architecture," *Opt. Lett.*, vol. 44, no. 11, pp. 2819–2822, 2019.
- [4] O. Avaya, E. Almeida, Y. Prior, and T. Ellenbogen, "Composite functional metasurfaces for multispectral achromatic optics," *Nature Commun.*, vol. 8, no. 1, 2017, Art. no. 14992.
- [5] T. Roy, S. Zhang, I.W. Jung, M. Troccoli, F. Capasso, and D. Lopez, "Dynamic metasurface lens based on MEMS technology," *APL Photon.*, vol. 3, no. 2, 2018, Art. no. 021302.
- [6] F. Ding, A. Pors, and S.I. Bozhevolnyi, "Gradient metasurfaces: A review of fundamentals and applications," *Reports Progress Phys.*, vol. 81, no. 2, 2018, Art. no. 026401.
- [7] H. T. Chen, A. J. Taylor, and N. F. Yu, "A review of metasurfaces: Physics and applications," *Reports Progress Phys.*, vol. 79, no. 7, 2016, Art. no. 076401.
- [8] H. Yang *et al.*, "Reflective metalens with sub-diffraction-limited and multifunctional focusing," *Scientific Reports*, vol. 7, no. 1, 2017, Art. no. 12632.
- [9] D. Y. Lu *et al.*, "Broadband reflective lens in visible band based on aluminum plasmonic metasurface," *Opt. Express*, vol. 26, no. 26, pp. 34956–34964, 2018.
- [10] S. Y. Zhang *et al.*, "High efficiency near diffraction-limited mid-infrared flat lenses based on metasurface reflectarrays," *Opt. Express*, vol. 24, no. 16, pp. 18024–18034, 2016.
- [11] S. Wang *et al.*, "Broadband achromatic optical metasurface devices," *Nature Commun.*, vol. 8, no. 1, 2017, Art. no. 187.
- [12] F. Ding, Y. T. Chen, and S. I. Bozhevolnyi, "Gap-surface plasmon metasurfaces for linear-polarization conversion, focusing, and beam splitting," *Photon. Res.*, vol. 8, no. 5, pp. 707–714, 2020.
- [13] A. I. Kuznetsov, A. E. Miroshnichenko, M. L. Brongersma, Y. S. Kivshar, and B. Luk'yanchuk, "Optically resonant dielectric nanostructures," *Science*, vol. 354, no. 6314, 2016, Art. no. 2472.
- [14] S. Kruk, B. Hopkins, I. I. Kravchenko, A. Miroshnichenko, D. N. Neshev, and Y. S. Kivshar, "Invited Article: Broadband highly efficient dielectric metadevices for polarization control," *APL Photon.*, vol. 1, no. 3, 2016, Art. no. 030801.
- [15] A. Rahimzadegan *et al.*, "Beyond dipolar Huygens' metasurfaces for full-phase coverage and unity transmittance," *Nanophotonics*, vol. 9, no. 1, pp. 75–82, 2020.
- [16] H. K. Shamkhi *et al.*, "Transverse scattering and generalized kerker effects in all-dielectric mie-resonant metaoptics," *Phys. Rev. Lett.*, vol. 122, no. 19, 2019, Art. no. 193905.
- [17] N. F. Yu *et al.*, "Light propagation with phase discontinuities: Generalized laws of reflection and refraction," *Science*, vol. 334, no. 6054, pp. 333–337, 2011.
- [18] Y. Q. Yang *et al.*, "Multimode directionality in all-dielectric metasurfaces," *Phys. Rev. B*, vol. 95, no. 16, 2017, Art. no. 165426.
- [19] N. Li *et al.*, "Large-area metasurface on CMOS-compatible fabrication platform: Driving flat optics from lab to fab," 2020. [Online]. Available: <https://www.degruyter.com/view/journals/nanoph/ahead-of-print/article-10.1515-nanoph-2020-0063/article-10.1515-nanoph-2020-0063.xml?language=en>
- [20] S. Zhang *et al.*, "Solid-immersion metalenses for infrared focal plane arrays," *Appl. Phys. Lett.*, vol. 113, no. 11, 2018, Art. no. 111104.
- [21] J.-S. Park *et al.*, "All-Glass, large metalens at visible wavelength using deep-ultraviolet projection lithography," *Nano Lett.*, vol. 19, no. 12, pp. 8673–8682, 2019.
- [22] J. R. Devore, "Refractive indices of rutile and sphalerite," *J. Opt. Soc. Amer.*, vol. 41, no. 6, pp. 416–419, 1951.
- [23] I. H. Malitson, "Interspecimen comparison of the refractive index of fused silica," *J. Opt. Soc. Amer.*, vol. 55, no. 10, pp. 1205–1209, 1965.
- [24] X. H. Ding *et al.*, "Reflectance bandwidth and efficiency improvement of light-emitting diodes with double-distributed bragg reflector," *Appl. Opt.*, vol. 56, no. 15, pp. 4375–4380, 2017.
- [25] M. Khorasaninejad *et al.*, "Polarization-insensitive metalenses at visible wavelengths," *Nano Lett.*, vol. 16, no. 11, pp. 7229–7234, 2016.
- [26] P. Grahn, A. Shevchenko, and M. Kaivola, "Electromagnetic multipole theory for optical nanomaterials," *New J. Phys.*, vol. 14, no. 9, 2012, Art. no. 093033.
- [27] W. Liu, A.E. Miroshnichenko, and Y.S. Kivshar, "Q-factor enhancement in all-dielectric anisotropic nanoresonators," *Phys. Rev. B*, vol. 94, no. 19, 2016, Art. no. 195436.
- [28] A.B. Evlyukhin, C. Reinhardt, A. Seidel, B.S. Luk'yanchuk, and B.N. Chichkov, "Optical response features of Si-nanoparticle arrays," *Phys. Rev. B*, vol. 82, no. 4, 2010, Art. no. 045404.
- [29] R. Alaei, R. Filter, D. Lehr, F. Lederer, and C. Rockstuhl, "A generalized Kerker condition for highly directive nanoantennas," *Opt. Lett.*, vol. 40, no. 11, pp. 2645–2648, 2015.
- [30] W. Liu and Y.S. Kivshar, "Generalized Kerker effects in nanophotonics and meta-optics [Invited]," *Opt. Express*, vol. 26, no. 10, pp. 13085–13105, 2018.
- [31] J. H. Zhang, M. ElKabbash, R. Wei, S. C. Singh, B. Lam, and C. L. Guo, "Plasmonic metasurfaces with 42.3% transmission efficiency in the visible," *Light-Sci. Appl.*, vol. 8, 2019, Art. no. 53.
- [32] A.B. Evlyukhin, C. Reinhardt, and B.N. Chichkov, "Multipole light scattering by nonspherical nanoparticles in the discrete dipole approximation," *Phys. Rev. B*, vol. 84, no. 23, 2011, Art. no. 235429.